Geophys. J. Int. (2009) **176,** 951–964 doi: 10.1111/j.1365-246X.2008.04035.x

Developing framework to constrain the geometry of the seismic rupture plane on subduction interfaces *a priori* – a probabilistic approach

Gavin P. Hayes* and David J. Wald

U.S. Geological Survey, National Earthquake Information Center, USA. E-mail: ghayes@usgs.gov

Accepted 2008 October 28. Received 2008 October 24; in original form 2008 August 1

SUMMARY

A key step in many earthquake source inversions requires knowledge of the geometry of the fault surface on which the earthquake occurred. Our knowledge of this surface is often uncertain, however, and as a result fault geometry misinterpretation can map into significant error in the final temporal and spatial slip patterns of these inversions. Relying solely on an initial hypocentre and CMT mechanism can be problematic when establishing rupture characteristics needed for rapid tsunami and ground shaking estimates.

Here, we attempt to improve the quality of fast finite-fault inversion results by combining several independent and complementary data sets to more accurately constrain the geometry of the seismic rupture plane of subducting slabs. Unlike previous analyses aimed at defining the general form of the plate interface, we require mechanisms and locations of the seismicity considered in our inversions to be consistent with their occurrence on the plate interface, by limiting events to those with well-constrained depths and with CMT solutions indicative of shallow-dip thrust faulting. We construct probability density functions about each location based on formal assumptions of their depth uncertainty and use these constraints to solve for the 'most-likely' fault plane.

Examples are shown for the trench in the source region of the M_w 8.6 Southern Sumatra earthquake of March 2005, and for the Northern Chile Trench in the source region of the November 2007 Antofagasta earthquake. We also show examples using only the historic catalogues in regions without recent great earthquakes, such as the Japan and Kamchatka Trenches. In most cases, this method produces a fault plane that is more consistent with all of the data available than is the plane implied by the initial hypocentre and CMT mechanism. Using the aggregated data sets, we have developed an algorithm to rapidly determine more accurate initial fault plane geometries for source inversions of future earthquakes.

Key words: Earthquake dynamics; Earthquake source observations; Seismicity and tectonics; Subduction zone processes.

1 INTRODUCTION

To understand many aspects of the rupture process of an earthquake, recent seismology has often used finite-fault source inversions, which tell us in (generally) high detail the spatial and temporal evolution of slip on a fault plane during an earthquake. A key component of these inversions – and indeed in many other aspects of seismological analysis – is an accurate knowledge of the geometry of the fault on which the earthquake occurred. However, the determination of the location and geometry of that surface is often approximate at best. It is commonly initially assumed that the fault surface conforms to the arcward-dipping fault plane of the best-fitting double couple mechanism of a centroid moment tensor solution (hereafter referred to as the corresponding CMT fault plane). However, this plane is frequently inconsistent with other *a priori* evidence, such as earthquake locations in historic catalogues of past hypocentres and CMT centroids, and surface fault-break locations. In addition this plane, when centred on the CMT centroid location, does not always pass through the body-wave arrival-time hypocentre of the current event. Subsequent use of such a fault plane in an earthquake source inversion may map fault geometry mislocation into error in the final temporal and spatial slip pattern.

Many of these inconsistencies arise as a result of uncertainties in earthquake location (particularly in depth) which, for example, can contain errors of as high as several tens of kilometres in the National Earthquake Information Center (NEIC) Preliminary Determination of Epicentres (PDE) catalogue (Engdahl *et al.* 1998;

*Contracted by Synergetics, Inc. (www.synergetics.com).

Dewey *et al.* 2007), one of the main data sources for this study. Inconsistencies between CMT centroid locations and earthquake hypocentres also result from characteristics of the seismic waveform from which each location type is derived. Hypocentre locations in the NEIC PDE are derived using short-period ($T < 1$ s) body waves, while CMT solutions (e.g. those in the global CMT; gCMT; catalogue, http://www.globalcmt.org) are based on waveform fits to long-period body waves ($T > 40$ s) and surface waves ($T > 100$ s). The different frequency contents of these waves give rise to sensitivity to different attributes of the earthquake rupture process and faulting history (Lay & Wallace 1995). In general terms, the hypocentre is often considered the locus of slip initiation while the CMT location represents the 'centroid' of the total fault moment release or slip. Despite these differences, however, the locations derived from each solution should theoretically represent points on the same fault surface, if that surface is planar. If an earthquake involves motion on a non-planar surface whose components have significantly different geometries, the CMT solution will represent the average or dominant geometry. Under these assumptions, we can use each solution to aid in the representation of the fault surface.

Since high quality seafloor bathymetry and gravity data sets have become available (e.g. Smith & Sandwell 1997; Arko *et al.* 2007; Marine Geoscience Data System, http://www.marine-geo.org), several efforts have been made to map out the precise locations of global plate boundaries (e.g. Bird 2003; Tarr *et al.* 2009). As a result, we know the locations of major surface fault breaks (e.g. seafloor trench locations) and thus have an additional constraint on the fault plane location and geometry for earthquakes that occur on the plate boundary interface.

In this study, we improve upon existing assumptions of fault plane geometry for earthquake source inversions by utilizing the abundant data available in catalogues of historic seismicity. We constrain the geometry of the seismic rupture plane of subducting slabs by combining historic earthquake hypocentre and centroid locations and the location of the trench break on the seafloor. The 'best' location for each individual event is used for this constraint, selected from a hierarchy of catalogues whose ranking is based on location uncertainty. We construct probability density functions (PDFs) about each location based on formal assumptions of their depth accuracy and use these constraints to solve for the 'most-likely' fault plane. We solve for a single-planar fault surface, as it is planar geometries that are assumed in the majority of earthquake source inversion procedures in use today. This method can easily be adapted to accommodate multiplane, curved or non-planar geometries if the *a priori* data warrant additional complexity, and as the need for such complex geometries arises in earthquake source modelling. This increased level of detail will benefit from the use of further *a priori* constraints, such as those from active seismic surveys across the trench.

Previous studies have attempted to model Wadati–Benioff Zone (WBZ) geometry in subduction zones, particularly near volcanic arcs (e.g. England *et al.* 2004; Syracuse & Abers 2006). However, such studies were principally concerned with identifying the structure of slabs at intermediate depths beneath volcanic arcs, and thus describe slab geometry deeper than the shallow seismogenic interface of primary interest in this study. For example, Syracuse & Abers (2006) fit hand-drawn contours to seismicity at depths greater than 50 km, while England *et al.* (2004) studied intermediate-depth seismicity, between 80–400 km. Furthermore, these studies did not formally attempt to restrict seismicity distributions used to constrain the WBZ surface to those earthquakes with subduction mechanisms, because at intermediate depths it has been shown that the average depth to seismicity approximately represents the depth to the slab surface to within a few kilometres error (e.g. Zhao *et al.* 1997).

In this study, we focus on the shallow, seismically active part of the slab surface in the upper ∼60–80 km, modelling only that part of the subduction zone likely to rupture in future megathrust events. We combine several earthquake catalogues and restrict events analysed to those whose mechanisms match that expected for a subduction thrust rupture. We constrain our modelled interface to pass through the location of the trench on the seafloor, which is well known. In reality, the rupture plane likely lies some kilometres below the seafloor at the trench, beneath a layer of incoming sediment or within the oceanic crust itself. However, as trench sediment thicknesses are not universally well known, we choose to constrain our most-likely interface at the trench location on the seafloor for simplicity. Further analysis and discussion of this assumption is included in Section 5. Finally, we incorporate formal uncertainty estimates regarding location depths to produce a model of the shallow slab interface geometry (the seismogenic fault plane) that is consistent with all the data available to us, rather than subsets of this information. Our principle goal is not to produce a model that precisely describes the 3-D structure of subduction interfaces, but rather to present a way to improve upon existing models and assumptions of interface structure that are used in earthquake source inversions—one of the main research products produced after any major subduction thrust earthquake. By improving such fault structure models, we can in turn facilitate the improvement of subsequent source inversions, enabling a more accurate assessment of slip distribution immediately after an earthquake occurs.

Examples of our approach are shown for the Sumatra Trench near Nias Island, which has experienced several large earthquakes over the last few years, and for the Northern Chile Trench near Antofagasta, which ruptured in a M_w 7.8 earthquake in November 2007. We also show examples using only the historic catalogues in regions without recent great earthquakes, such as the Kamchatka and Japan Trenches. In all cases, this method leads to a fault plane that is most consistent with all of the seismic and bathymetric data used. Using the aggregated data sets, we have developed an algorithm to determine *a priori* a more accurate fault plane geometry for source inversions of future earthquakes than is otherwise available.

2 PROCEDURE TO CONSTRAIN SLAB INTERFACE GEOMETRY

This approach calculates the most-likely orientation (strike ϕ and dip δ) and depth of a planar approximation to the shallow, seismogenic portion of the subducting plate interface at the location of the users' choice (hereafter referred to as the 'reference location') by incorporating data from historic earthquake catalogues (gCMT, NEIC PDE and the global relocation catalogue of Engdahl *et al.* (1998), hereafter labelled EHB), locations of trench breaks on the seafloor (from the plate boundary files of Tarr *et al.* 2009) and any 'new' event location (both NEIC hypocentre and gCMT centroid). The latter data are incorporated specifically for situations where the user wishes to constrain fault plane geometry prior to an earthquake source inversion of a recent event, and can be omitted where inappropriate. In situations in which a new event is used, its epicentroid becomes the reference location, and the resulting interface geometry can be used to infer a 'most-likely' depth of the event assuming it ruptured the plate interface. Aside from the reference location, there are no differences between the two approaches.

Our earthquake catalogue selection criteria are explained graphically in Fig. 1. Initially, earthquake catalogues are merged by

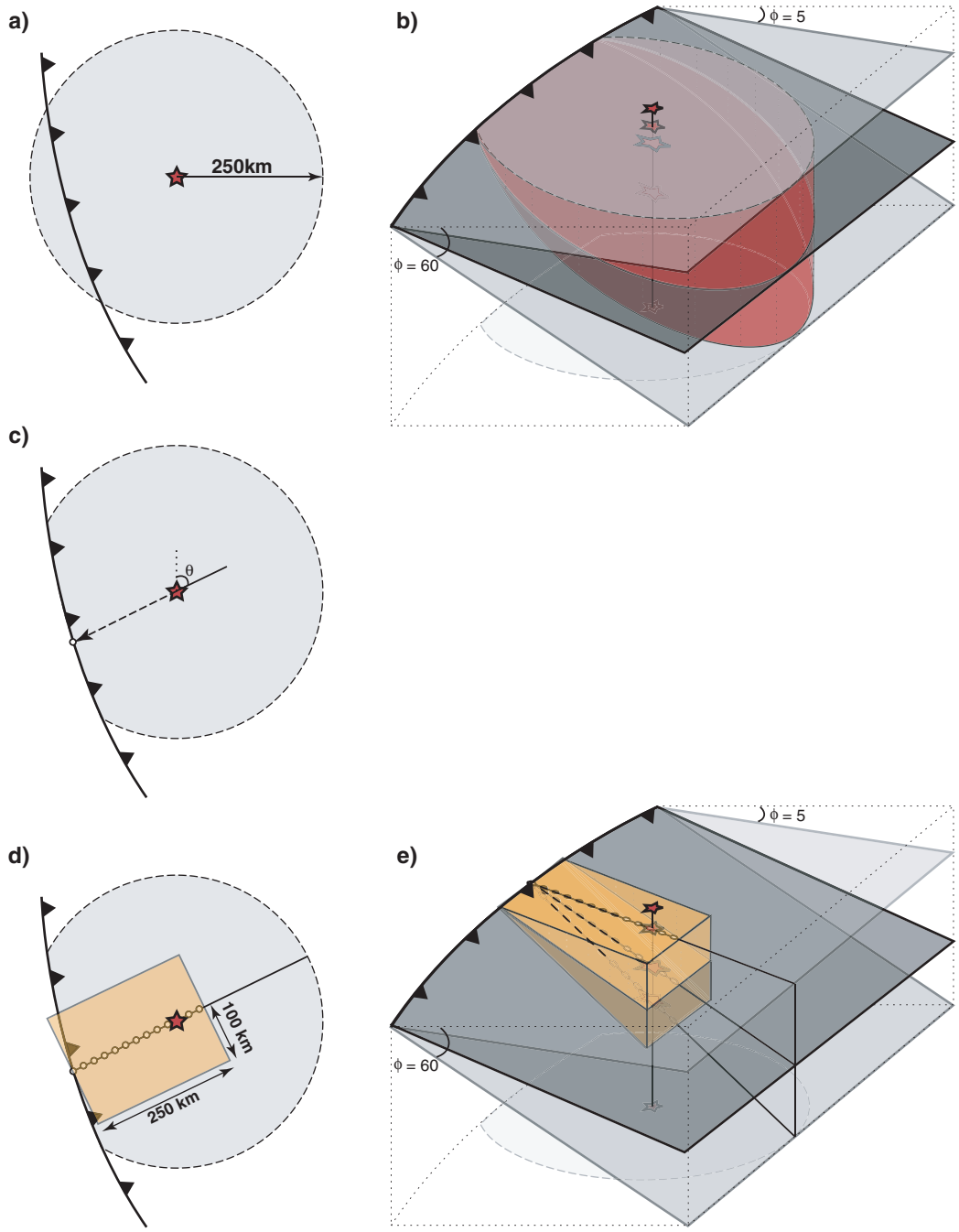

Figure 1. Schematic diagram describing event selection and filtering prior to geometry constraint. (a) Step 1: all well-constrained (Frohlich & Davis 1990) events from the gCMT catalogue with thrust mechanisms, and within 250 km of the reference location (red star) are selected. (b) Step 2: all events shallower than the equivalent depth of a plane dipping 5°, and steeper than the equivalent depth of a plane dipping 60°, at the same distance from the trench are removed from the catalogue, thereby reducing the influence of upper-plate and deep earthquakes from the inversion. Events outboard of the trench are removed. The maroon shaded region represents the remaining region of events. (c) Step 3: using the remaining mechanisms, the average CMT strike is calculated. The perpendicular to the strike (θ) is assumed to represent the approximate angle of subduction in this region of the subduction zone. From the reference location (red star), and using this angle (θ), we project back to the nearest point on the trench to establish the starting point of our reference profile. (d) Step 4: using the trench location and angle θ from (c), we construct the reference profile, from 0 to 250 km perpendicular to the average CMT strike. At this stage, all events greater than 100 km distance from the reference profile in a direction perpendicular to that profile are removed. The remaining region of events, in map view, is shaded orange. (e) Representation of the final step (d) in 3-D perspective. Events in this volume constitute data used for the subsequent fault plane geometry search (see text for details).

matching event location and origin times. This merged catalogue is then filtered in an attempt to restrict events used in our geometry constraint to those earthquakes that represent rupture on the subduction thrust, under the following criteria:

(1) Hypocentre location is within approximately 250 km of the reference location (i.e. potentially on the shallow, seismogenic part of the plate interface; Fig. 1a).

(2) The CMT solution is well constrained, following the criteria proposed by Frohlich & Davis (1990). Though these criteria reduce the size of the useable gCMT catalogue by 50 per cent, the remaining solutions have uncertainties in nodal plane parameters of just 5°–10°.

(3) Fault and auxiliary plane rake angles match that expected for a thrust or oblique-thrust mechanism ($30^\circ < \lambda < 150^\circ$).

(4) Hypocentre depth is greater than a shallowly dipping thrust interface (set at 5°), and shallower than that of a steeply dipping thrust interface (60°), at the equivalent distance from the trench. See Fig. 1(b). This step removes obvious upper-plate and deep seismicity, restricting our catalogue to subduction-related events.

In the next step, we use these filters to constrain the regional subduction strike direction by computing the average strike of all CMTs from the gCMT catalogue that match the above criteria (Fig. 1c). While some events unrelated to subduction may pass these filters, the majority are removed: thus the filtered seismicity data set is dominated by subduction thrust events.

Having constrained the subduction strike direction, in the third step we construct a reference profile for the subduction zone in question (Fig. 1d). The trench location is chosen by first sampling every 1 km along the local plate boundary (Tarr *et al.* 2009), and then finding the trench position closest to the reference (user-defined) location in a direction perpendicular to the strike of the subducting plate. This trench location and strike direction combine to produce the reference profile for all subsequent calculations. Depth to the seafloor at this location is calculated by interpolating bathymetry data (Arko *et al.* 2007; Marine Geoscience Data System, http://www.marinegeo.org) to the location of the trench. At this stage, two final filtering procedures are performed, constraining the useable catalogue further to pre-selected events within ∼100 km of the surface projection of the reference profile in a direction normal to that profile, whose strike (for both nodal planes) approximately matches (±30°) the subduction direction (Fig. 1e).

In the fourth step, we introduce locations from the EHB and NEIC catalogues for those earthquakes from the gCMT catalogue that passed all of these filters. Events from the EHB and NEIC catalogues are not chosen if they do not have a corresponding gCMT location, as we require information on the mechanism of the earthquake to increase our confidence that they represent the subduction process. Furthermore, EHB events are not used if their depth is not considered well constrained, as determined by solution type information reported in the catalogue (Engdahl *et al.* 1998). Each individual event is considered only once in the inversion process; its location is selected from the available reporting agencies (EHB, NEIC and gCMT) in a hierarchical order based on event epicentral error—thus if EHB locations are available, they are used, followed by NEIC locations, and finally gCMT locations. This ordering is chosen because, even for relatively small ($M < 7$) events whose source dimensions are small and thus whose epicentroid should correspond to the epicentre, horizontal offsets between the EHB and gCMT catalogues average ∼31 km globally, compared to ∼9 km between the EHB and NEIC locations. This order also follows more detailed analyses by Engdahl *et al.* (1998). In practice, because PDE locations are available for all events that have a CMT solution (for locations analysed in this study), centroid locations from the gCMT catalogue are never used, and therefore in future discussion we refer only to EHB and NEIC epi- or hypocentre locations.

In the fifth step, we incorporate location uncertainty by constructing normal distribution PDFs for each event location. For those events selected, all epicentres are considered known, as their errors are in general small in comparison to fault dimensions and depth errors—as are the depth, location and orientation of the trench. Earthquake depths are considered uncertain, and are assigned PDFs centred in the Z-axis on the reported depth from the locations' source catalogue, and in the X-axis on the epicentre. The width (standard deviation) of each PDF is determined by the depth uncertainty reported or calculated for that event.

In addition to qualitative descriptions of focal-depth accuracy, the EHB catalogue reports standard errors in depth, which are retained to define the variance of the PDF of each EHB location used. Variance is set as the square of the standard error. For the NEIC catalogue, a constant error of ±18 km is assigned, based on the average vertical uncertainty computed from a comparison between the global EHB and NEIC catalogues. Weighting is also included in the final solution. Individual event weighting is assigned according to the square of the event magnitude, with larger events receiving higher weighting, as these events are more likely to rupture the plate interface.

Finally, we compute the dip of the subduction zone perpendicular to the direction of average strike by fitting an inclined plane through the pre-computed PDFs of the selected event locations. We follow a maximum likelihood approach to calculate the probability of the plane dipping at an angle ranging from $\delta = 5^\circ$ to $\delta = 60^\circ$, bounding likely scenarios for the shallow seismic sections of all global subduction zones, according to the following formula:

$$P(\delta) = \prod_{i=1}^{i=n} \left\{ \left[\frac{1}{\sigma_i \sqrt{2\pi}} \exp \left\{ -\frac{[x(\delta) - \mu_i]^2}{2\sigma_i^2} \right\} \right] w_i + \omega \right\}, \qquad (1)$$

where σ is the variance of the PDF, $x(\delta)$ defines the depth of the plane dipping δ° at a distance x km from the trench, μ the expected (reported) depth, w the individual weighting for event i and ω is a water level used to circumvent problems caused by calculated depths having a probability of zero for any given event. This water level is set at $\omega = 0.1$ for all inversions. Eq. (1) can be transformed into a sum by taking the logarithm of individual probabilities, as follows (Eq. (2)):

$$P'(\delta) = \sum_{i=1}^{i=n} \log \left\{ \left[\frac{1}{\sigma_i \sqrt{2\pi}} \exp \left\{ -\frac{[x(\delta) - \mu_i]^2}{2\sigma_i^2} \right\} \right] w_i + \omega \right\}. \qquad (2)$$

This step circumvents issues encountered when taking the product of a large number of near-zero probabilities. To establish that results are not heavily influenced by outliers or the specific method used to calculate the most-likely interface dip, we also calculate the geometry of the best-fitting plane following weighted least-squares and singular value decomposition (SVD) approaches. These calculations result in the most probable single-plane geometry of the subduction thrust interface near the reference location that is consistent with the seismicity data and intersects the Earth's surface at the trench.

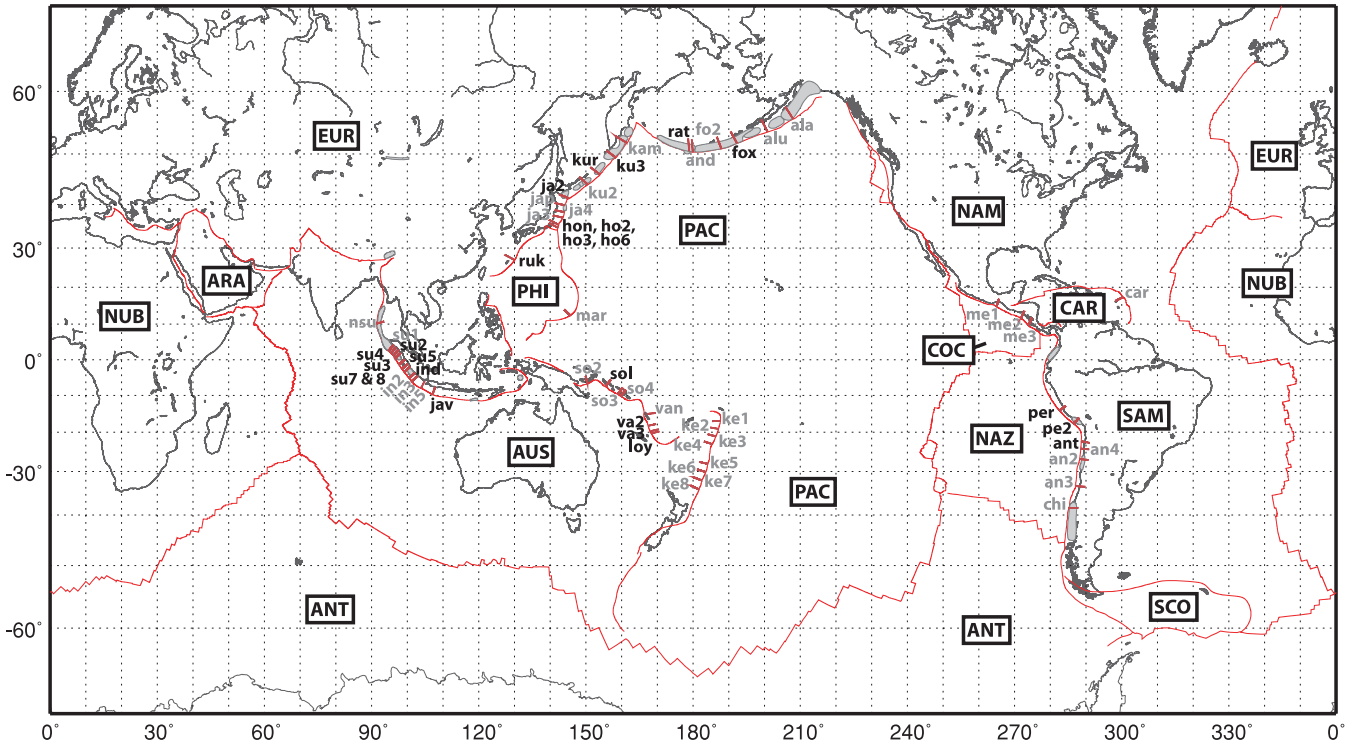

Figure 2. Global map of subduction zones studied in this analysis. Lower case three-letter codes and maroon profiles identify areas where subduction zone geometry has been constrained. Bold codes are constrained with a 'new' event; grey codes use historic catalogues only. Boxed capital letters identify tectonic plate codes. Rupture zones of historic great earthquakes are shaded grey (Tarr *et al.* 2009). Global plate boundaries are shown in red, from Tarr *et al.* (2008).

3 GEOMETRIES OF GLOBAL SUBDUCTION ZONES

This procedure has been tested in seismically active subduction zones worldwide. Four examples are shown here—others can be found in the Appendix S1. A summary of all locations that have been analysed to date is given in Fig. 2. In the first two examples shown here (Nias Island and Antofagasta), hypocentroid/centre locations of a 'new event' are included as additional constraint in the inversion; in subsequent examples (Kamchatka and Japan), we use historic catalogues alone.

First, we show results near Nias Island, above the Sumatra subduction zone that ruptured in an M_w8.6 earthquake on 2005 March 28, using the M_w 6.2 Nias Islands earthquake of 2008 January 22 (∼50 km further south of the 2005 event) as a 'new event'—thus including complete historic catalogues up to that date. The aftershock sequence of the 2005 earthquake adds significant data to the inversion, and thus provides stronger constraints on the solution. Our inversion solves for a fault plane striking at an angle of 318°N (constrained by 76 gCMT observations) and dipping 9° towards the northeast (constrained by 27 EHB and 15 NEIC locations). Despite having a similar depth (within 3 km) as the best-fitting subduction interface at the epicentroid location, the corresponding fault plane of the gCMT solution for this event had a dip of 23°NE. This is much steeper than our inversion suggests, steeper than suggested by the trend in background seismicity, and inconsistent with the location of the trench on the seafloor (Fig. 3). The gCMT solution strike was 334°N, which is a reasonable fit to our most-likely fault plane. The maximum likelihood probability function across a range of trial dips from 5° to 60° is sharply and narrowly peaked at 9° (Fig. 3b), within ±2° of the least-squares and SVD solutions for the same data set.

Similar results are found when inverting for trench geometry with the 2005 earthquake as a 'new event', using historic catalogues inclusive through 2005 March 27 only. In this case, our inversion solves for a fault plane striking at an angle of 303°N (constrained by 29 gCMT observations), dipping 10° towards the northeast (constrained by five EHB and two NEIC locations; see Appendix S1). The probability function for this event demonstrates a similar sharp and narrow peak. Comparing these results to those shown in Fig. 3 shows strong consistency between locations and data sets, and implies that, for this location, a small subset of data (2005 event; Appendix S1) accurately describes the structure defined by a more complete data set (Fig. 3). If such an observation holds globally, it becomes important for areas that experience lower rates of seismic activity and/or have longer seismic cycles such that our current catalogues are incomplete.

The variation in dip of the fault planes of CMT solutions used as constraints in the inversion for the M_w 6.2 2008 event versus distance along fault plane cross-section is shown in Fig. 3d. We have averaged these dips into 20 km bins along the cross-section, via a bulk average and also by weighting each dip by the seismic moment of the event. This plot is useful for several purposes. First, it shows that although there is considerable variation in dip across the area of the trench considered here (ranging from ∼8° to ∼38°), this variation does not appear systematic—for example, dip does not increase with distance from the trench in this shallow portion of the plate interface, as we would expect for deeper portions of the WBZ. This again indicates that our assumption of a single plane used for computation simplicity is probably appropriate here. Second, this plot also illustrates that the majority of CMT solutions considered have corresponding fault planes that dip at steeper angles than does the 'most-likely' planar subduction interface. While bulk averages show that this difference appears somewhat random, the weighted

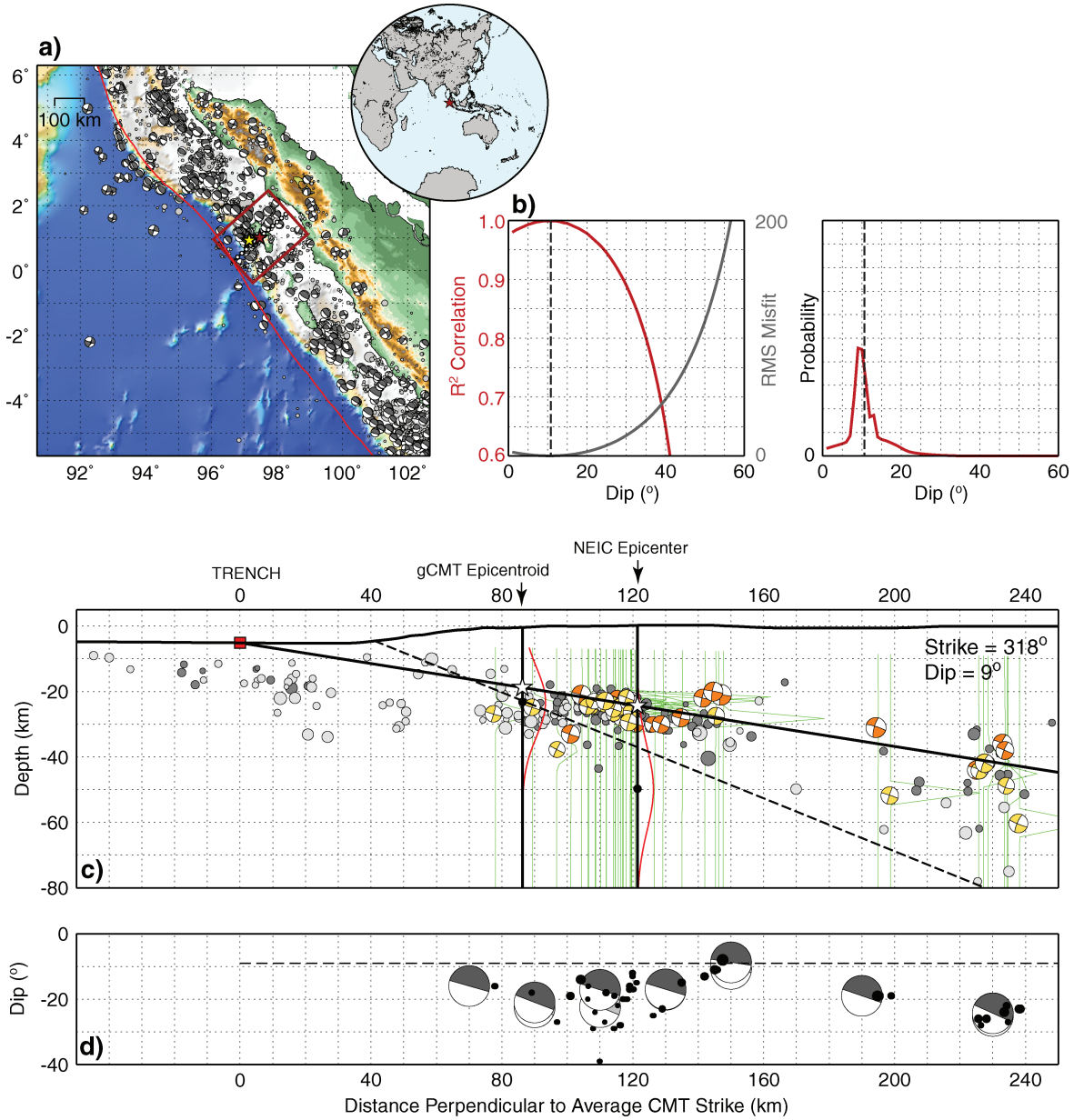

Figure 3. Maps describing the subduction interface geometry constraint for the Sumatra Trench at the location of the 2008 January 22 M_w 6.2 Nias Islands earthquake. (a) Basemap of Sumatra subduction zone showing the area of the trench constrained in this example. Earthquake locations from the gCMT catalogue (focal sphere mechanisms) and NEIC catalogue (grey circles, sized according to magnitude) are shown. Red rectangle indicates the area shown in cross-section (c); all earthquakes within this area may be used to constrain trench geometry. Red star indicates reference (new earthquake) location; yellow star represents equivalent gCMT centroid location for reference event. (b) Probability functions describing interface dip likelihood over a range of dips from 0° to 60°. The right-hand panel describes results from a maximum likelihood approach; the left-hand panel for weighted least squares (red and grey solid lines) and SVD (dashed black vertical line). (c) Cross-section of subduction zone taken perpendicular to the average strike of gCMTs that match selection criteria and whose equivalent EHB or NEIC locations lie within the orange box from (a). Gold CMTs are mechanisms from the gCMT catalogue plotted at their equivalent EHB catalogue location, used to constrain trench strike and dip. Orange CMTs are mechanisms without EHB locations, placed instead at the equivalent event location in the NEIC catalogue, and also used to constrain geometry. Light and dark grey circles are events from the EHB catalogue south and north of the plane of the cross-section, respectively. Those not overlain with CMTs as described above are not used to constrain geometry because either (i) they did not have a corresponding mechanism in the gCMT catalogue or (ii) their mechanism in the gCMT catalogue did not match selection criteria. The trench location is marked with a red square, and labelled 'Trench'. Probability density functions for EHB and NEIC locations are shown as green lines, scaled by a factor of ×20 for display purposes. The black solid line describes the best-fitting geometry. The initial locations of the 'new event' used to help constrain geometry are shown by black circles and marked with arrows corresponding to the gCMT epicentroid and NEIC epicentre. PDFs for these locations are shown in red; the most-likely depth for each location is marked with a white star, at the intersection of the most-likely subduction interface plane and the gCMT centroid/NEIC epicentre location. The best-fitting fault plane from the gCMT catalogue for the new event is shown with a black dashed line. (d) Variation in dip of best-fitting fault planes from the gCMT catalogue for all events used to constrain trench geometry across the plane of the cross-section. Individual event dips are shown with small dark grey circles, sized with magnitude. Large mechanisms indicate the average dip in 20 km bins across the plane of the cross-section. Light grey mechanisms represent a bulk average; dark grey represents a moment-weighted average.

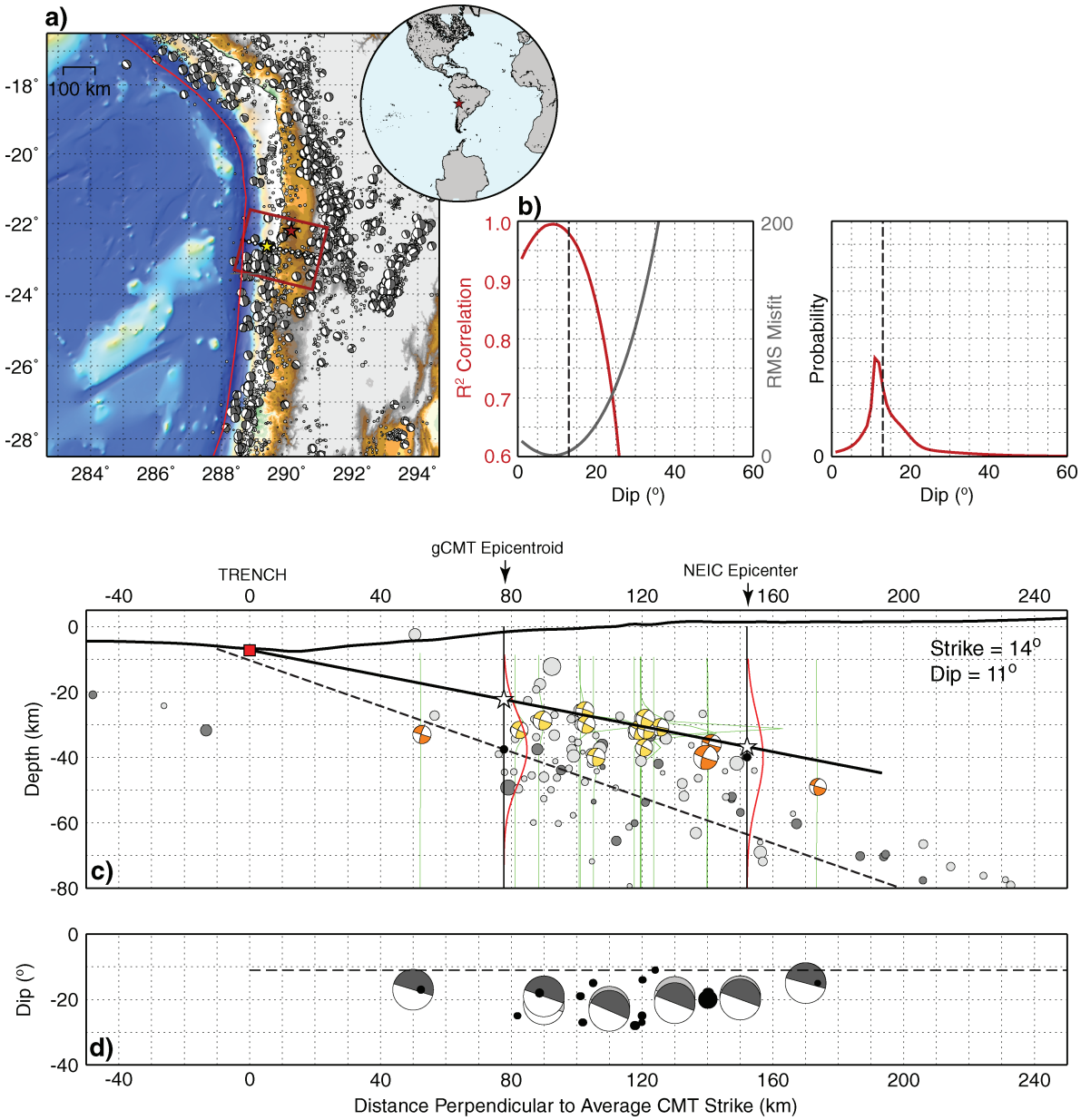

Figure 4. Maps describing the subduction interface geometry constraint for the Northern Chile Trench at the location of the 2007 November 14 M_w 7.8 Antofagasta earthquake. See Fig. 3 caption for descriptions of all symbols and labels. (a) Basemap of Northern Chile subduction zone showing the area of the trench constrained in this example. (b) Probability function describing interface dip likelihood. (c) Cross-section of subduction zone taken perpendicular to the average strike of gCMTs, used to constrain trench interface dip. (d) Variation in dip of best-fitting fault planes from the gCMT catalogue for all events used to constrain trench geometry across the plane of the cross-section.

averages suggest that this difference may be a function of earthquake size, with bigger events rupturing fault planes more closely aligned with the subduction interface (Fig. 3d). These observations are reasonably consistent across each of the subduction zones we have analysed, and will be expanded upon in the Section 5 of this paper.

Our second example is centred near the Antofagasta area of the Northern Chile subduction zone that ruptured in an M_w 7.8 earthquake on 2007 November 14 (Fig. 4). This earthquake is used as the reference location, and thus we utilize the complete catalogue up to and including 2007 November 13 in our analysis. Recurrence rates of moderate-sized earthquakes (i.e. those with gCMT mechanisms) are lower here than in other areas studied, and as a result fewer events pass our selection criteria. In the vicinity of the reference event, 30 earthquakes from the gCMT catalogue constrain the strike of the trench at an angle of 014°. Of these, 10 EHB and four NEIC locations constrain interface dip to an angle of 11° towards the east. Despite fewer events used in the constraint of the most-likely plane, the probability function is unimodal and strongly peaked at 11° (Fig. 4b), again within ±2° of the least-squares and SVD solutions. The corresponding fault plane of the gCMT solution for this event had a dip of 20°E, steeper than our inversion suggests, and steeper than suggested by the trend in background seismicity, though this seismicity is somewhat diffuse. The strike of the

best-fitting gCMT plane was 358°, slightly more northerly than suggested in our inversion. The most-likely depth we obtain for the NEIC epicentre (depth to the interface at the epicentral location) is almost identical to the reported depth in the NEIC PDE catalogue (37 km versus 40 km), while the depth of the interface at the epicentroid location is ∼15 km shallower than the reported depth of the event in the gCMT catalogue.

As with our first example in Sumatra, dips of the event mechanisms along the plane of this cross-section are consistently steeper than is the dip of the most-likely subduction interface (Fig. 4d). Perhaps because of the lower levels of recorded seismicity here, no trend is apparent in these dip discrepancies. Also, larger events do not show a tendency to align more closely with the interface as they do in Sumatra, possibly the result of a lack of large events in the time window considered (all events used to constrain the geometry near Antofagasta have $M_w \leq 6.0$, with the exception of the reference 2007 November 14 event).

Subduction interface geometry in the region of the M_w 9.0 1952 November 4 Kamchatka earthquake is shown in Fig. 5. Here, we use the complete historic catalogue (1976–present, constrained by the limit of the gCMT catalogue) to constrain the interface geometry, and do not consider any 'new' event for additional constraint. Our inversion determines a fault plane striking at an angle of 213° (constrained by 99 gCMT observations), dipping 14° towards the northwest (constrained by 37 EHB and nine NEIC locations). The probability function over the 5°–60° range is unimodal, and strongly peaked at 14°, the same dip suggested by both least-squares and SVD approaches (Fig. 5b). This plane is visually well correlated with background seismicity. The epicentre of the 1952 megathrust event, and its mechanism (Kanamori 1976) are plotted on the cross-section (Fig. 5c), but are not used for constraint in the inversion as the event depth is likely highly uncertain—the dip of this mechanism (30°) and location of the event (in both the EHB and NEIC catalogues) are inconsistent with the locations of background seismicity, the trench and our most-likely fault plane.

Interestingly, as with our previous examples, Fig. 5(d) shows that the corresponding fault planes of the majority of gCMT mechanisms are consistently steeper than the geometry of the subduction interface. These mechanisms demonstrate dips of ∼20°–40°, in contrast to our most-likely plane dip of 14°, and are visually inconsistent with the trend of both EHB and NEIC catalogue locations (Fig. 5c). In Kamchatka, this difference in dip does not show as striking a dependence on event size as does the 2008 Nias Island event source region; here gCMT dips are consistently ∼15° steeper across the region analysed. Differences in dip also seem to increase slightly with depth and distance from the trench, suggesting the slab interface may be beginning to roll over near ∼130 km. Even taking such a roll over in consideration, however, gCMT dips remain steeper than the subduction interface.

Our fourth and last example is centred on the Japan Trench subduction zone in northern Honshu, near 40.0°N, 143.5°E (Fig. 6). As with the Kamchatka trench example, here we constrain subduction interface geometry using the historic catalogues alone. In the vicinity of our reference location, 130 events from the gCMT catalogue matched selection criteria and constrain the subduction interface strike at 195°. Of these, 37 EHB and 14 NEIC locations constrain interface dip as 14°E (Fig. 6b and c). As with previous examples, the probability function for this inversion demonstrates a sharp, unimodal peak, whose result is consistent with that from least-squares and SVD methods. This most-likely planar geometry demonstrates an excellent agreement with the slab geometry inferred from local data sets (shown in Fig. 6 as a dashed line; Hasegawa *et al.* 1994).

Dips of the corresponding gCMT fault planes match our interface dip more closely in Japan than in other regions analysed (Fig. 6d). In the shallowest portion of the slab (within ∼100 km of the trench), gCMT dips are distributed about the 14° dip of our most-likely plane. Between ∼100 and 200 km distance from the trench, gCMT dips cluster, on average, ∼10° steeper than our plane. This could suggest that the slab begins to roll over to steeper angles in this region; however, the trends in locations of the EHB events (both those used to constrain the trench geometry and others not selected) correspond to our most-likely plane and do not appear to demonstrate such roll over (Fig. 6c), suggesting some other explanation may be required to account for discrepancies between gCMT fault plane dips and interface geometry.

4 DIP DISCREPANCY

In the majority of the subduction zones we have studied, we have observed often substantial differences between the dip of our inverted slab interface and the dips of the best-fitting fault planes of the gCMT mechanisms for the events that occur on or close to that plane (Figs 3d, 4d, 5d and 6d, and Appendix S1). This observation is summarized in histogram format in Fig. 7(a), comparing interface dip geometry from our inversions and gCMT mechanism dips for all events used to constrain geometry at all subduction zone cross-sections studied. This histogram shows fairly broad scatter, with a standard deviation of ∼8°, and a definite negative bias (i.e. interface geometries at shallower angles than are gCMT mechanisms along each section), with a mean of ∼ –9°, raising the question of what causes such a discrepancy in dips between individual events and overall subduction structure. We offer some suggestions here.

It is possible that these differences in dip arise from errors and uncertainties in the CMT inversion process. Particularly at shallow depths where thrust faulting often involves shallow structures ($\lesssim$30 km), the dip of CMT solutions is poorly constrained using long-period surface waves because of a trade-off between moment and dip; as such, small changes in dip for low-angle absolute dips can result in a change in moment by as much as a factor of 2 (e.g. Kanamori & Given 1981; Banerjee *et al.* 2005). Depending on the inversion process, it is possible that such a trade-off could lead to a bias towards an overestimation of dip in favour of a more stable moment. However, the persistence of observations of dip discrepancy throughout the depth range analysed at each subduction zone (0 km to ∼80 km) would suggest that at least for the deeper events for which trade-off between dip and moment is not severe, this artefact is not the cause of the observed discrepancies. Furthermore, comparisons with mechanisms derived from the NEIC moment tensor catalogue (http://neic.usgs.gov/neis/FM/fast_moment.html) and NEIC broad-band solutions (Choy, private communication, 2008) show the same distributions of dip discrepancies, suggesting the cause is either not related to the inversion technique itself, or is associated with methodologies used in all types of inversions.

CMT inversion techniques (as well as other standard earthquake location procedures) are also likely biased by the 1-D velocity models they assume, particularly at subduction zones, where velocity structure is clearly not 1-D. Such bias influences the hypocentral location of earthquakes in global catalogues that use teleseismic observations, tending to shift locations arcward and downdip of their true positions (Engdahl, private communication, 2008). Because we anchor our inverted best-fitting planes at the trench, these location biases may cause an underestimation of the true dip of the subduction interface. However, analysis of these bias effects along the

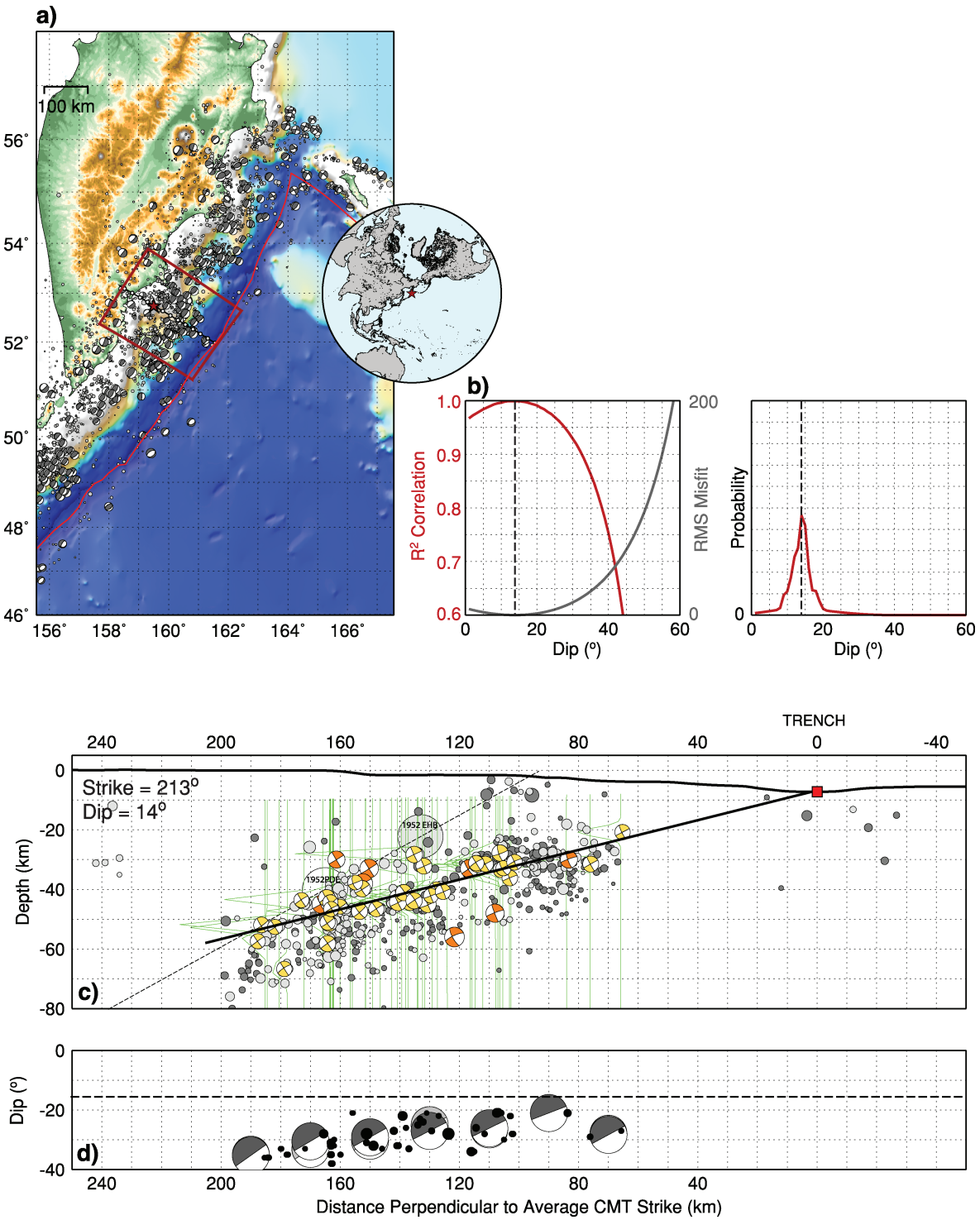

Figure 5. Maps describing the subduction interface geometry constraint for the Kamchatka Trench near the great *M* 9.0 1952 earthquake. See Fig. 3 caption for descriptions of all symbols and labels. (a) Basemap of Kamchatka subduction zone showing the area of the trench constrained in this example. (b) Probability function describing interface dip likelihood. (c) Cross-section of subduction zone taken perpendicular to the average strike of gCMTs, used to constrain trench interface dip. (d) Variation in dip of best-fitting fault planes from the gCMT catalogue for all events used to constrain trench geometry across the plane of the cross-section.

Sumatra, Japanese and Aleutians arcs shows that shifting events by as much as 15–30 km trenchward and 5–10 km updip only introduces a 1°–2° of steepening to the most-likely fault plane, much smaller than is needed to explain the majority of discrepancy between individual event best-fitting mechanism dip angles and the dip of the subduction interface. Furthermore, analysis of the distributions of hypocentres independently located with a local OBS and land-based array near Simeulue (Engdahl, private communication, 2008) show compatibility with our best-fitting interface structure in that region, providing further confidence in our inversion results.

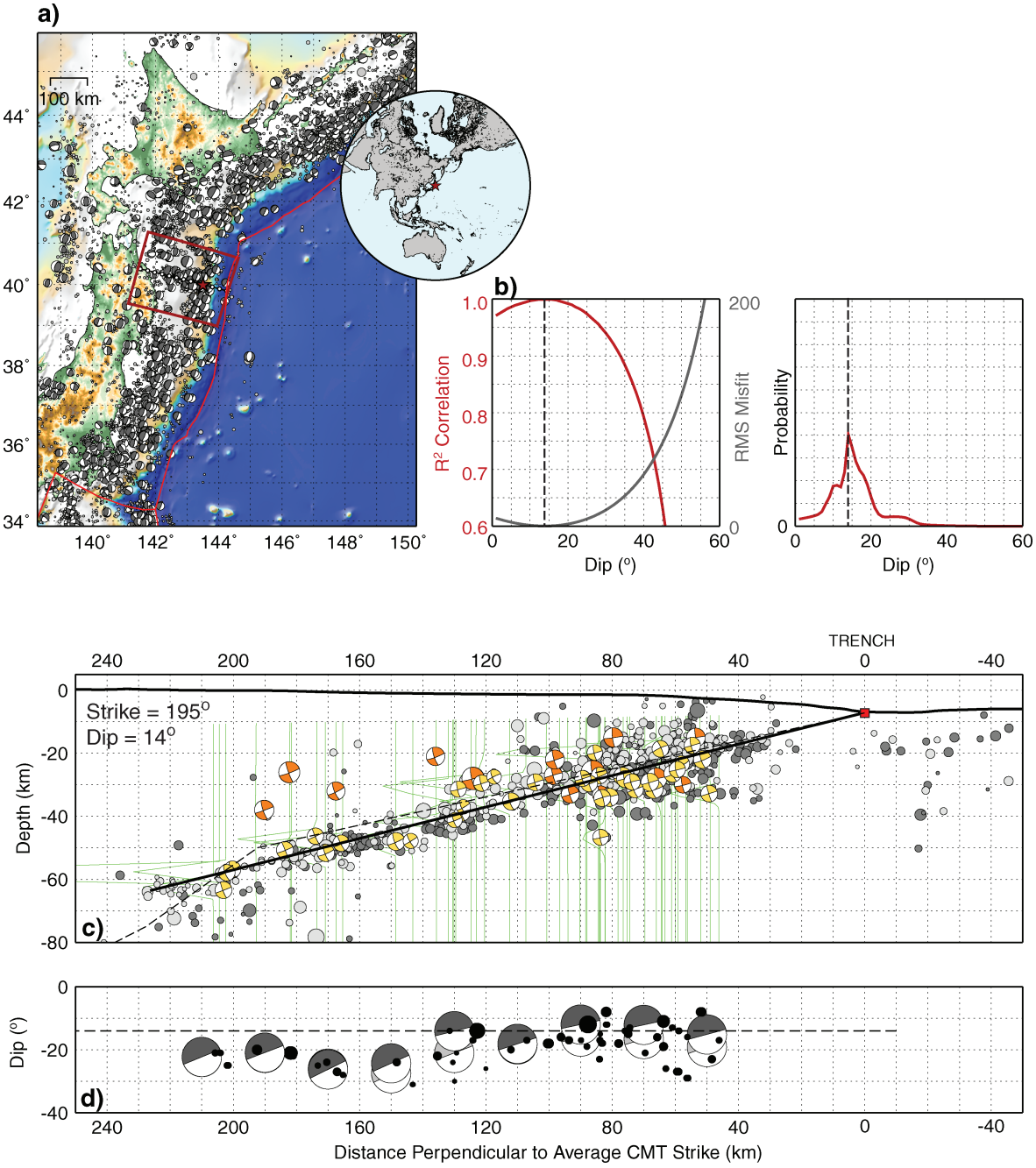

Figure 6. Maps describing the subduction interface geometry constraint for the Japan Trench near 40.0°N, 143.5°E. See Fig. 3 caption for descriptions of all symbols and labels. (a) Basemap of Japan subduction zone showing the area of the trench constrained in this example. (b) Probability function describing interface dip likelihood. (c) Cross-section of subduction zone taken perpendicular to the average strike of gCMTs, used to constrain trench interface dip. Dashed line represents the upper seismic plane surface of Hasegawa *et al.* (1994), Fig. 3, projected into the plane of this cross-section. (d) Variation in dip of best-fitting fault planes from the gCMT catalogue for all events used to constrain trench geometry across the plane of the cross-section.

Similarly in northern Japan, our interface matches well with the slab surface of Hasegawa *et al.* (1994), inferred from locally recorded and relocated seismicity using land and OBS network data (Fig. 6). The addition of similar data sets, where available, will help to further constrain our results worldwide.

An alternative explanation is that these discrepancies in dip for events across the entire depth range studied are (at least in part) real signals, and are evidence for rupture on structures (generally more steeply) inclined with respect to the subduction interface, on which smaller subduction-related events can occur. The mechanisms of these events could thus be rotated with respect to that expected for events occurring on the subduction interface itself. On the other hand, megathrust events rupture the 'true' interface, and thus their mechanisms have fault plane dip angles the same as or close to that of the slab. Such a model can explain the observation (near Nias Island; Fig. 3) that differences in dip may be a function of earthquake size. Lack of such moment-dependency in other subduction zone examples studied here may be a result of a deficiency of large

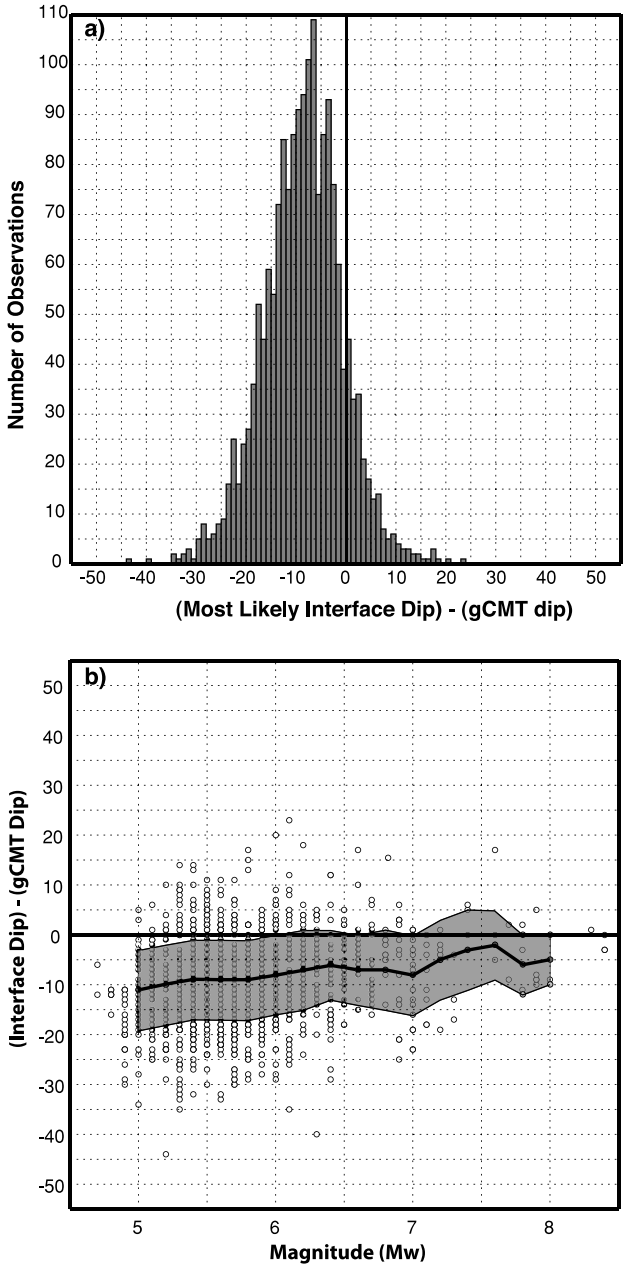

Figure 7. (a) Histogram describing the difference in dip between our inverted interfaces and the individual mechanisms of moment tensor solutions for earthquakes along (and/or close to) those interfaces, for all studied subduction zones globally. These results imply a bias towards steeper gCMT solution dips than inferred by our geometry inversions. In (b), we show this discrepancy as a function of magnitude. White circles show individual observations; the dark line represents the average discrepancy for ($M_w \pm$ 0.5 magnitude units), and the grey shaded region describes one standard deviation from that mean, suggesting a gradual trend towards higher magnitude earthquake mechanisms aligning more closely with the inferred subduction interface dip.

earthquakes in these locations over the time interval studied, rather than a difference in behaviour (e.g. both areas of the Kamchatka and Japanese arcs studied here have not had an earthquake with $M > 8$ in at least the past 30 yr, while in Antofagasta all events considered have $M \leq 6$, with the exception of the reference 2007 November 14 event). Moment-dependency on a global basis is explored in Fig. 7(b), which shows that in general, over all subduction zones analysed in this study, larger magnitude events have gCMT dips closer to the dip inferred from our subduction zone geometry analysis inversion.

The latter model may be related to observations of systems of steeply dipping thrust faults in accretionary wedges (e.g. Davis *et al.* 1983; Dahlen 1990; Bangs *et al.* 2004; Wang & Hu 2006) at deeper levels of the subduction thrust, ideas of a finite width to a fault/deformation zone (e.g. Sibson 1977; Otsuki 1978; Hull 1988; Tsutsumi *et al.* 2004) and/or subduction channels (e.g. Shreve & Cloos 1986; Beaumont *et al.* 1999; Bachmann 2008), rather than one single fault plane along which all motion between two sides of a fault is accommodated. In the framework of such models, our observations may suggest that in the seismogenic portion of a subduction zone, earthquakes often occur on inclined structures adjacent to the main subduction thrust, representing small releases of moment which accommodate small percentages of the plate motion, while larger events occur on the main through-going fault interface itself – their size dictates their rupture occurs on a continuous structure, able to harbour large offsets – and accommodate the major part of long-term seismic motions.

Regardless of causative mechanism, the observation of discrepancy in dip between the inferred subduction interfaces from this study and the individual mechanism dips of earthquakes along those interfaces is striking, and merits further exploration. Solving the issue may provide more understanding of the uncertainties involved in moment tensor inversions, earthquake locations, and possibly the dynamics of the subduction thrust itself, and the distribution of earthquakes around that interface.

5 DISCUSSION AND CONCLUSION

This work presents a new approach towards constraining the interface geometry of the shallow, seismogenic portion of subducting slabs using information from a selection of historic global earthquake catalogues, seafloor trench locations and probabilistic assessments of errors in earthquake location depths. We fit this interface with a single-plane solution, which (based on the data we have analysed in this study) seems reasonable for this shallowest portion of the slab; typically only at deeper levels and at greater distances from the trench than those considered here does the slab begin to roll over to significantly steeper angles. In some cases, such as the Kamchatka example shown here (Fig. 5), small amounts of roll over are evident even in this seismogenic portion of the slab. Whether such locations would benefit from modelling with higher-degree polynomial fits is as yet unclear, and is currently being investigated in ongoing in-depth studies.

Some subduction zones also show evidence for very low dip (less than 10°) in the shallow, aseismic portion of the slab above the seismogenic interface region modelled in this study (e.g. Pacific Plate beneath NE Japan, Hasegawa *et al.* 1994; Pacific Plate beneath the Mariana arc, Oakley *et al.* 2008; Indian Plate beneath W Java, Kopp *et al.* 2002). In these cases, if slip were to propagate from where the earthquake nucleated into areas above the seismogenic zone, dips inferred from our inversion may overestimate the true dip of parts of the ruptured interface. While trade-offs between moment and dip (e.g. Kanamori & Given 1981) imply that an overestimation of dip would result in a comparable miscalculation of moment, it is impossible to represent these regions of slab interfaces

with the data sets currently available and used in this study. Furthermore, these areas are also not directly represented by the planar models currently in use for earthquake source inversions (i.e. the shallow plane of the best-fitting double couple to gCMT solutions). To improve the modelling of earthquakes that include rupture in the shallow aseismic zone, future earthquake source inversions may need to move away from the assumptions of planar interfaces that are currently adopted. When such steps are made, we can also begin to integrate models of the shallow aseismic slab structure (e.g. from active seismic data that image the plate boundary near the trench) in our inversions, and accurately represent the changes in geometry of the entire subduction interface from trench to deep seismicity.

The inclusion of data from the shallow sections of subduction zones will also allow the explicit consideration of sediment thickness at the trench. At present, we use the simplistic assumption that the most-likely interface intersects the Earth's surface at the trench break on the seafloor, rather than beneath a column of sediment of (in most cases) unknown thickness. As active surveys likely image both the top and bottom of such sediment packages, this mismatch can be accounted for when such data are included. In our current approach, relaxing weighting on the trench location by a factor of 100 shifts the average depth of the interface at the trench (i.e. at $x = 0$ km) by –5 km, suggesting data may be consistent with a sediment column beneath the trench. However, we do not explore such models further using current planar geometry assumptions because these models overparametrize our inversion and as a result the dip of the interface at greater depths – in the seismogenic zone, the main target for this study – is poorly constrained and in general significantly underestimated. As more data become available and polynomial geometry interface models become viable, we can account for such affects.

The examples we have presented (Figs 3–6), and those included in additional Appendix S1 (locations summarized in Fig. 2), show that in general, in areas where background seismicity rates for moderate–large events (i.e. those with mechanisms in the gCMT catalogue) are sufficiently high, this method is able to resolve the most-likely interface geometry with high confidence. Complications arise where seismicity is diffuse (e.g. Cascadia, Nankai, Caribbean and Southern Chile), depth uncertainty is large and thus locations are scattered (e.g. some parts of the Southern Hemisphere versus the more densely instrumented Northern Hemisphere), and where seismogenic zone seismicity is not easily resolved from upper-plate earthquakes. Examples of such cases can be seen in the Solomon Islands (near the 2007 April 1 $M_{\rm w}$ 8.1 earthquake; Appendix S1), where the subducting slab rolls over very quickly after entering the trench, and in the Kuril Islands (near the /2006 November 15 $M_{\rm w}$ 8.3 earthquake; Appendix S1), where upper-plate seismicity levels appear high. Our examples also show that in some areas, even when historic seismicity catalogues are incomplete (e.g. the area around the Nias Islands 2005 event prior to that earthquake, as discussed earlier), this method can confidently resolve the same geometry as does an inversion with a more complete data set (Fig. 3). Fig. 2 summarizes the complete set of trench locations and geometries analysed in this study on a global tectonic map, each labelled with a unique three-letter descriptive code.

The resolution of the geometry of the subducting slab interface allows us to constrain fault plane parameters (strike and dip) as *a priori* information in earthquake source inversions of large megathrust events, under the assumption that these events likely rupture part of that same thrust interface. Currently these inversions (e.g. finite-fault inversions produced at the NEIC) typically use a planar starting model based on the best-fitting fault plane from CMT inversions, centreed on the preliminary hypocentre from the NEIC catalogue. Both can contain significant error and tend to be inconsistent with one another; the fault plane may not pass simultaneously through the CMT centroid location, the initial NEIC hypocentre, and the trench location, three points that should all lie on the same plane for a single event (assuming a planar fault). This error is mapped into uncertainty and bias in the final solution of the source inversion, implying that slip distributions inferred from these models are not as accurate as they could be. Such uncertainty may have significant implications for hazard analyses based on inversion results. However, by using *a priori* constraints on fault geometry garnished from analysing 40 yr worth of complementary earthquake location data sets, we can remove much of this uncertainty and create more reliable source inversion models.

We show an example of this effect in Fig. 8, a finite-fault inversion of the $M_{\rm w}$ 7.8 2007 November 14 Antofagasta, Chile earthquake (geometry constraint shown in Fig. 4). All models shown are constructed using the finite-fault inverse algorithm of Ji *et al.* (2002). Fig. 8(a) describes results from a finite-fault inversion using fault geometry constrained by the gCMT solution ($\phi = 358^\circ$, $\delta = 20^\circ$, $\lambda = 98^\circ$), centred at the initial NEIC catalogue hypocentre (22.19°S, 69.84°W, 60.0 km depth), the first iteration for this event solution performed immediately after the event at the NEIC. Constraining the fault plane in the hypocentral region of this event using *a priori* information from previous seismicity (as described in this study), implies fault geometry of $\phi = 011^\circ$, $\delta = 12^\circ$. Subsequent finite-fault inversion results, using this fault plane geometry at a hypocentre centred on the depth to this interface at the epicentral location (∼39 km), are shown in Fig. 8(b). Moment rate functions for the two models are shown in Fig. 8(c). Model 1 implies three similarly sized, large pulses of moment release at ∼10, ∼30 and ∼60 s, while the second model describes two pulses of moment release at ∼10 and ∼30 s, peak slip in the second pulse, and no major slip asperity beyond 30 s.

The differences between these two models are significant, particularly for the slip patch concentrated at the event hypocentre, which moves ∼20 km shallower in the latter model. Though the surface projections of major slip patches do not change a great deal between models, their depth distributions change substantially because of the shallower fault plane used in the second inversion. These results become significant for any subsequent models that rely on the depth and distribution of slip in earthquakes inferred from these types of finite-fault inversions, such as ground shaking estimates upon which response decisions are based (e.g. Wald *et al.* 2006; Earle & Wald 2007). These model dip differences would also likely be resolvable in data sets such as those from observations of surface uplift (e.g. coral uplift studies, Briggs *et al.* 2006), near-field GPS networks (e.g. Banerjee *et al.* 2007) or tsunami inundation measurements (e.g. Fujii & Satake 2007). However, these data sets are not typically available immediately after an earthquake occurs, and as such rapid response requires establishing accurate constraints with *a priori* data.

Using the *a priori* data readily available in historic earthquake catalogues, and the new geometry inversion technique presented in this study, we have shown that we are able to accurately solve for subduction interface geometry in a broad selection of global subduction zones. Furthermore, we have shown that these interfaces better reflect the distribution of past seismicity and potential future megathrust earthquakes than do the best-fitting double couples of single moment tensor inversions, and thus they provide a more robust starting point for earthquake source inversions and related hazard analyses.

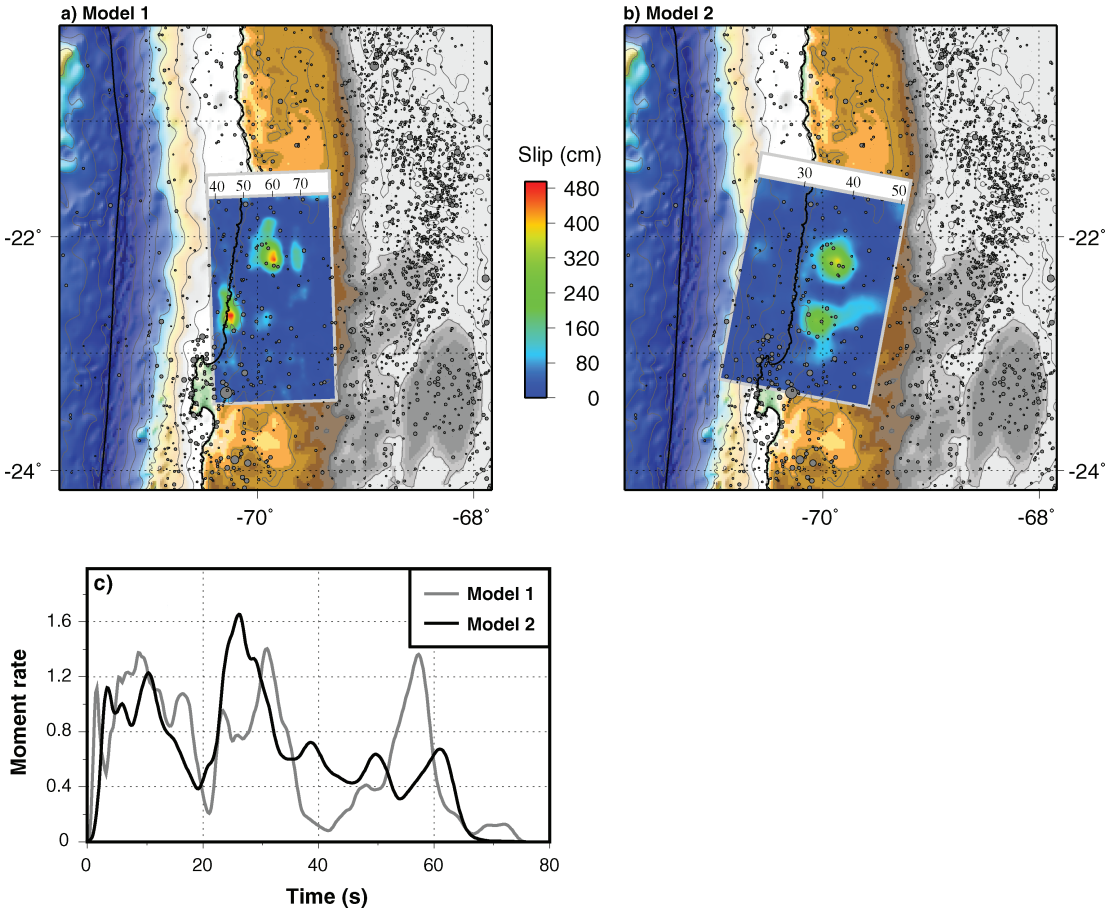

Figure 8. Finite-fault inversions demonstrating the change in modelled slip distributions using fault planes based on (a) the gCMT best-fitting fault plane at the initial NEIC catalogue hypocentre and (b) the most-likely fault plane from our probabilistic subduction interface inversion. These models constrain the slip history of the earthquake based on the finite-fault inverse algorithm of Ji *et al.* (2002), analysing 13 teleseismic broad-band *P* waveforms, six broad-band SH waveforms and 23 long-period surface waves selected based upon data quality and azimuthal distribution. In each figure, the surface projection of the fault plane used in the inversion is coloured based on slip amplitude. The scale at the top of each model relates to the depth distribution of the fault plane. Dark grey circles represent background seismicity up to the day prior to this event, scaled by magnitude. The thick black lines represent the plate boundary and the coastline; light grey lines represent contours of bathymetry data (from the Marine Geoscience Data System, http://www.marine-geo.org) at 1000 m intervals. (c) Moment-rate time functions for each finite-fault model, in units of 10^{19} N m s^{-1}.

ACKNOWLEDGMENTS

We thank Anthony Lomax and two anonymous reviewers for their comments. We also thank Richard Briggs, James Dewey, Bob Engdahl, Stephen Kirby, Chen Ji and Kevin Furlong for helpful comments and discussions during the preparation of this manuscript. Many of the figures were made using GMT, and we thank their developers and the many users of their support list. Finally, we thank Bob Engdahl and the Global Centroid Moment Tensor Group for the maintenance of and open access to their respective earthquake catalogues.

REFERENCES

Arko, R., Ryan, W. *et al*., 2007. The global multi-resolution topography (GMRT) synthesis, *EOS, Trans. Am. geophys. Un.,* **88**(52), Fall Meet. Suppl., Abstract IN51B-0405.

Banerjee, P., Pollitz, F.F & Bürgmann, R., 2005. The size and distribution of the Sumatra-Andeman earthquake from far-field static offsets, *Science,* **308,** 1769–1771.

Banerjee, P., Pollitz, F.F, Nagarajan, B. & Bürgmann, R., 2007. Coseismic slip distributions of the 26 December 2004 Sumatra-Andaman and the 28 March 2005 Nias earthquakes from GPS static offsets, *Bull. seism. Soc. Am.,* **97,** S86–S102.

Bangs, N.L., Shipley, T.H., Gulick, S.P.S., Moore, G.F., Kuromoto, S. & Nakamura, Y., 2004. Evolution of the Nankai Trough décollement from the trench into the seismogenic zone: inferences from three-dimensional seismic reflection imaging, *Geology,* **32,** 273–276.

Beaumont, C., Ellis, S. & Pfiffner, A., 1999. Dynamics of sediment subduction-accretion at convergent margins: short-term modes, long-term deformation, and tectonic implications, *J. geophys. Res.,* **104,** 17 573–17 602.

Bird, P., 2003. An updated digital model of plate boundaries, *Geochem. Geophys. Geosyst.,* **4,** 1–52.

Briggs, R.W. *et al*., 2006. Deformation and slip along the Sunda megathrust in the great Nias-Simeulue earthquake, *Science,* **311,** 1897–1901.

Dahlen, F.A., 1990. Critical taper model of fold-and-thrust belts and accretionary wedges, *Ann. Rev. Earth Planet. Sci.,* **18,** 55–99.

Davis, D., Suppe, J. & Dahlen, F.A., 1983. Mechanics of fold-and-thrust belts in accretionary wedges, *J. geophys. Res.,* **88,** 1153–1172.

Dewey, J.W., Choy, G., Presgrave, B., Sipkin, S., Tarr, A.C., Benz, H., Earle, P. & Wald, D., 2007. Seismicity associated with the Sumatra–Andaman Islands earthquake of December 26, 2004, *Bull. seism. Soc. Am.,* **97,** S25–S42.

Earle, P.S. & Wald, D.J., 2007. PAGER-Rapid Assessment of an Earthquake's Impact, U.S. Geological Survey Fact Sheet 2007–3101, 4 pp.

Engdahl, E.R., Van Der Hilst, R.D. & Buland, R.P., 1998. Global teleseismic earthquake relocation with improved travel times and procedures for depth determination, *Bull. seism. Soc. Am.,* **88,** 722–743.

England, P., Engdahl, R. & Thatcher, W., 2004. Systematic variation in the depths of slabs beneath arc volcanoes, *Geophys. J. Int.,* **156,** 377–408.

Frohlich, C. & Davis, S.D., 1990. How well constrained are well-constrained T, B, and P axes in moment tensor catalogs? *J. geophys. Res.,* **104,** 4901–4910.

Fujii, Y. & Satake, K., 2007. Tsunami source of the 2004 Sumatra-Andaman earthquake inferred from tide gauge and satellite data, *Bull. seism. Soc. Am.,* **97,** S192–S207.

Hasegawa, A., Horiuchi, S. & Umino, N., 1994. Seismic structure of the northeastern Japan convergent margin: a synthesis, *J. geophys. Res.,* **99,** 22 295–22 311.

Hull, J., 1988. Thickness – displacement relationships for deformation zones. *J. Struct. Geol.,* **10,** 431–435.

Ji, C., Wald, D.J. & Helmberger, D.V., 2002. Source descriptions of the 1999 Hector Mine, California, earthquake, part I: wavelet domain inversion theory and resolution analysis, *Bull. seism. Soc. Am.,* **92,** 1192–1207.

Kanamori, H., 1976. Re-examination of the Earth's free oscillations excited by the Kamchatka earthquake of November 4, 1952, *Phys. Earth. planet. Inter.,* **11,** 216–226.

Kanamori, H. & Given, J.W., 1981. Use of long-period surface waves for rapid determination of earthquake-source parameters, *Phys. Earth. planet. Inter.,* **27,** 8–31.

Kopp, H., Klaeschen, D., Flueh, E.R. & Bialas, J., 2002. Crustal structure of the Java margin from seismic wide-angle and multichannel reflection data, *J. geophys. Res.,* **107,** doi:10.1029/2000JB000095.

Lay, T. & Wallace, T.C., 1995. *Modern Global Seismology,* Academic Press, San Diego, CA.

Oakley, A.J., Taylor, B. & Moore, G.F., 2008. Pacific Plate subduction beneath the central Mariana and Izu-Bonin fore arcs: new insights from an old margin, *Geochem. Geophys. Geosyst.,* **9,** Q06003, doi:10.1029/2007GC001820.

Otsuki, K., 1978. On the relationship between the width of shear zone and the displacement along fault. *J. Geol. Soc. Jpn.,* **84,** 661–669.

Shreve, L.R. & Cloos, M., 1986. Dynamics of sediment subduction, mélange formation, and prism accretion, *J. geophys. Res.,* **91,** 10 229–10 245.

Sibson, R.H., 1977. Fault rocks and fault mechanisms, *J. geol. Soc. Lond.,* **133,** 191–213.

Smith, W.H.F. & Sandwell, D.T., 1997. Global sea floor topography from satellite altimetry and ship depth soundings, *Science,* **277,** 1956–1962.

Syracuse, E.M. & Abers, G.A., 2006. Global compilation of variations in slab depth beneath arc volcanoes and implications, *Geochem. Geophys. Geosyst.,* **7,** Q05017, doi:10.1029/2005GC001045.

Tarr, A.C., Villaseñor, A., Benz, H.M. & Furlong, K.P., 2009. *Seismicity of the Earth 1900–2007, U.S. Geological Survey.* Scientific Investigations Map XXXX, 1 sheet, scale 1: 25,000.000.

Tsutsumi, A., Nishino, S., Mizoguchi, K., Hirose, T., Uehara, S., Sato, K., Tanikawa, W. & Shimamoto, T., 2004. Principal fault zone width and permeability of the active Neodani fault, Nobi fault system, southwest Japan, *Tectonophysics,* **379,** 93–108.

Wald, D.J., Earle, P.S., Lin, K., Quitoriano, V. & Worden, C.B., 2006. Challenges in rapid ground motion estimation for the prompt assessment of global urban earthquakes, *Bull. Earthq. Res. Inst.,* **81,** 273–281.

Wang, K. & Hu, Y., 2006. Accretionary prisms in subduction earthquake cycles: the theory of dynamic Coulomb wedge, *J. geophys. Res.,* **111,** doi:10.1029/2005JB004094.

Zhao, D., Matsuzawa, T. & Hasegawa, A., 1997. Morphology of the subducting slab boundary in the northeastern Japan arc, *Phys. Earth planet. Inter.,* **102,** 89–104.

SUPPORTING INFORMATION

Additional Supporting Information may be found in the online version of this article:

Appendix S1. Each page of this appendix describes the subduction interface geometry for a specific global subduction zone.

Please note: Wiley-Blackwell are not responsible for the content or functionality of any supporting materials supplied by the authors. Any queries (other than missing material) should be directed to the corresponding author for the article.